IVYSPRING INTERNATIONAL PUBLISHER

Theranostics

2027; 17(2): 716-733. doi: 10.7150/thno.139082

Research Paper

Pair production tomography enables imaging of MeV-scale gamma-emitting theranostic radionuclides

Biswajit Das[1,2], Robin Peter[3,1], Javier Caravaca[2,1], Youngho Seo[1,4,5]✉

1. Department of Radiology and Biomedical Imaging, University of California, San Francisco, California 94143, USA.
2. Nuclear Science Division, Lawrence Berkeley National Laboratory, Berkeley, California 94720, USA.
3. Department of Radiation Oncology, University of California, San Francisco, California 94143, USA.
4. Department of Nuclear Engineering, University of California, Berkeley, California 94720, USA.
5. Molecular Biophysics and Integrated Bioimaging Division, Lawrence Berkeley National Laboratory, Berkeley, California, 94720, USA.

✉ Corresponding author: Email: youngho.seo@ucsf.edu.

© 2027 The Author(s). This is an open access article distributed under the Creative Commons Attribution 4.0 International Licence, subject to the Publisher's Terms of Use at https://ivyspring.com/terms.

Received: 2026.06.09; Accepted: 2026.10.23; Published: 2027.01.01

Abstract

Rationale: MeV-scale gamma emissions present in the decay chains of certain therapeutic radionuclides can degrade image quality in conventional SPECT because of increased scatter and septal penetration. PET imaging offers sensitivity and energy discrimination benefits but is limited to positron-emitting isotopes. Pair production tomography (PPT) addresses this limitation by enabling localization of high-energy γ rays: when a γ ray with energy ≥ $2m_e c^2$ (1.022 MeV) undergoes pair production, it generates an e^+e^- pair, and the positron subsequently annihilates, emitting two coincident 511 keV photons that can be detected for tomographic reconstruction. In this work, we experimentally demonstrate PPT in the context of ^{212}Pb-targeted alpha therapy by exploiting the 2.617 MeV gamma emission from its decay daughter ^{208}Tl.

Methods: ^{212}Pb-filled phantoms were imaged using clinical time-of-flight and preclinical non-time-of-flight PET/CT systems, with SPECT/CT acquired for comparison. Additional high-statistics and TOF versus non-TOF PPT reconstructions were performed. Monte Carlo simulations characterized the positron transport, spatial localization, pair-production efficiency, tissue effects, and gamma-energy dependence.

Results: PPT images were experimentally demonstrated from 2.617 MeV γ emission of ^{208}Tl using both clinical TOF and preclinical non-TOF PET systems. Increased event statistics improved PPT image quality, visualization of smaller insert and SNR, while TOF reconstruction improved the PPT images. Monte Carlo simulations demonstrated that pair-production and annihilation events retain spatial information of source distribution and revealed tissue and energy-dependent differences in localization and pair-production efficiency of MeV-scale γ emitting radionuclides.

Conclusions: This study establishes the feasibility of pair-production tomography using the 2.617 MeV γ emission from ^{208}Tl in the ^{212}Pb decay chain. Further improvements in scanner sensitivity and timing performance may improve image quality and quantitative accuracy, motivating the future translation of PPT for theranostics imaging.

Keywords: targeted alpha therapy, ^{212}Pb daughter imaging, pair-production tomography, non-positron emitter PET imaging, MeV range gamma imaging and Monte Carlo simulation

Introduction

Nuclear medicine imaging has become a key component of modern healthcare by enabling noninvasive assessment of physiological and molecular processes *in vivo*, supporting diagnosis, treatment planning, and therapy monitoring [1-7]. In addition to the tens of millions of nuclear medicine imaging procedures performed each year worldwide, the past decade has witnessed a major expansion in the clinical use of radionuclides for cancer therapy [8-12]. The fact that many of these therapeutic radiopharmaceuticals also emit imageable γ-ray signatures has driven renewed interest in imaging technologies optimized for the theranostic setting [5,9,13-15]. Commercial Single Photon Emission Computed Tomography (SPECT) systems remain the standard for single γ-ray imaging but are optimized for

energies up to a few hundred keV [16-19] and exhibit degraded image quality at higher energies owing to increased scatter background and septal penetration, particularly for theranostic radionuclides with MeV-scale emissions in their decay chains [19-21]. Quantitative imaging of targeted alpha therapy (TAT) radionuclides and their daughters can be challenging because of limited imageable photon yields and image degradation caused by high-energy emissions from their decay chains. On the other hand, positron emission tomography (PET) offers highly sensitive and quantitative imaging of positron emitting radionuclides [4,22-23]. Modern PET systems achieve enhanced signal-to-noise ratio through fast timing resolution enabled by time-of-flight capabilities [24-28], and also through large axial field of view that provides high detection sensitivity [29-32]. However, most current clinical targeted alpha therapy radionuclides, including ^{212}Pb, ^{225}Ac, and ^{211}At, do not emit positrons suitable for conventional PET imaging, although exceptions such as ^{149}Tb have been reported [33,34].

Pair production provides a new route for imaging therapeutic radionuclides with PET systems without direct positron emission. When a gamma ray with energy $\geq 2m_e c^2$ (1.022 MeV) undergoes pair production, it generates an electron-positron e^+e^- pair; the positron subsequently annihilates, producing two coincident 511 keV photons that can be detected for tomographic reconstruction, as with PET. Internal pair production from an excited nuclear state, which is the direct emission of a e^+e^- pair without an intermediate photon, has been successfully explored for PET-like imaging of ^{90}Y through the 1.7 MeV excited state of ^{90}Zr [35-41]. Recent simulation studies have also proposed pair production tomography for *in vivo* dosimetry based on external MeV-range X-ray beams for radiotherapy [42,43]. Experimental investigation of pair-production tomography (PPT) using MeV-scale gamma emissions from therapeutic radionuclides remains limited.

One potential candidate for PPT imaging is ^{212}Pb, a promising radionuclide for TAT that is the focus of several clinical trials and experimental radiopharmaceutical developments [44-51]. ^{212}Pb decays through β^- emission to ^{212}Bi and emits multiple gamma rays, including 238.6 keV gamma commonly used for SPECT imaging. The daughter radionuclide, ^{212}Bi, subsequently decays through competing α (~36%) and β^- (~64%) branches; the latter populates the short-lived α emitter, ^{212}Po. Thus, the therapeutic α emissions arise from the daughter radionuclides in the ^{212}Pb decay chain rather than from ^{212}Pb itself. While essential for verification of TAT delivery to the target and assessment of off-target toxicity, the SPECT/CT imaging of ^{212}Pb using the 79 keV and 239 keV photon emissions has been demonstrated in both phantom and clinical studies [46,52-53]. However, as ^{212}Pb itself does not emit α particles, imaging of the parent radionuclide, whether direct or surrogate, introduces uncertainty in dose localization. Pharmacokinetic modeling and biological sampling can provide valuable information on daughter radionuclide redistribution, while imaging offers a direct, spatially resolved approach for assessing their *in vivo* distribution. A high energy gamma ray, 2.617 MeV, is emitted from a daughter nuclide ^{208}Tl with a probability of 36% per ^{212}Pb decay [54], motivating the investigation of PPT for imaging this emission. Recent related work presented at the EANM25 and TAT13 conferences demonstrated the feasibility of pair-production tomography using this emission in phantom and patient imaging [55,56]. However, systematic investigation of the underlying imaging characteristics, including pair-production localization, tissue dependence, and the role of time-of-flight detection, remains unexplored. PPT offers a fundamentally different technique for imaging high energy photon emissions that are poorly visualized with conventional medical scanners. In this context, the proposed approach is mainly motivated by three potential benefits: extending nuclear medical imaging beyond conventional energy ranges, investigating feasibility in TAT imaging using modern PET detection and coincidence-based discrimination, and enabling specific localization of the alpha emitting daughter of the ^{212}Pb decay chain.

Despite its promise, implementing PPT presents significant technical challenges. Pair production occurs less frequently than Compton scattering at this energy, and successful detection requires precise coincidence timing, higher sensitivity, detector materials with high stopping power, and robust event selection techniques to distinguish true pair production events from scattered background. Recent advances in detector technology, including high sensitivity total body PET systems such as EXPLORER [29,30], fast timing scanners [24-25,57], and improved reconstruction algorithms [25,58-59], have significantly advanced the field and pave the way for future adoption of this imaging approach.

In this work, we explored PPT imaging of the spatial distribution of ^{208}Tl, a daughter of ^{212}Pb, using 2.617 MeV gamma rays. Using both clinical and preclinical phantom studies with time of flight (TOF) PET and non-TOF PET systems configured for coincidence detection, we demonstrated the experimental tomographic imaging derived from pair production through gamma rays emitted by radionuclide. This work aims to investigate the

feasibility of pair production-based imaging for high-energy gamma emitters using Monte Carlo simulations and experimental phantom studies with clinical and preclinical PET systems. Ultimately, PPT may broaden the capabilities of nuclear medicine imaging and support accurate verification of emerging radionuclide therapies.

Methods and Results

^{212}Pb decay and principle of pair production tomography for imaging

In recent years, several ^{212}Pb-based radiopharmaceuticals have advanced into clinical development for targeted alpha therapy, including ^{212}Pb-DOTAMTATE for neuroendocrine tumors and ^{212}Pb-labeled PSMA agents for prostate cancer [44,45]. The decay chain of ^{212}Pb produces gamma emissions spanning energies from approximately 75 keV-2.7 MeV, as illustrated in **Figure 1**. One of its daughter radionuclides, ^{208}Tl, emits a high energy gamma ray, 2.617 MeV, from an excited state populated following beta decay, with a branching ratio of ~99%. In this work, we demonstrated PPT imaging of this daughter nuclide using the 2.617 MeV gamma ray. The pair production process for this gamma ray is illustrated schematically in the inset box of **Figure 2**. These high energy gamma rays interact with nuclei in tissue within the patient, positioned near the center of a ring-shaped PET detector array, producing an e^+e^- pair. Owing to its initial kinetic energy, the e^+ travels a short distance before losing energy. After coming to rest, the positron annihilates with an electron in the surrounding medium, producing two 511 keV photons emitted in opposite directions. Alternative annihilation channels, such as three photon emission, may also occur through ortho-positronium formation, although their branching probability is low [60-62]. The schematic of the proposed experimental PPT demonstration is illustrated in **Figure 2**.

Monte Carlo simulation

The attenuation length of the 2.617 MeV γ-ray in water is relatively long ($1/\mu \approx 23.4$ cm [63]). However, the event density of detected signal decreases with increasing distance from the source due to the combined effects of both attenuation and geometric spreading (as $\sim e^{-\mu r}/r^2$). At short distances, geometric spreading dominates this reduction, resulting in a strong localization of detected events around the source, while more distant interactions contribute primarily as low-level background. These effects were assessed in a series of homogeneous cube phantom simulations evaluating the kinetic energy (KE) distribution, range, production distance, and annihilation distance of the positron. Monte Carlo framework GATE 9.2 (Geant4) [64] was used to simulate $N = 10^8$ primary 2.617 MeV γ-rays emitted from a central isotropic source inside the cube. To quantify e^+/e^- kinetic energies and e^+ ranges, full particle histories were recorded in a 10 cm × 10 cm × 10 cm water cube. For pair production and annihilation profiles, larger 20 cm × 20 cm × 20 cm cubes were simulated with four materials: water, lung tissue, adipose tissue, and bone. Details about simulation geometry, physics lists, material composition, and interpretation, are provided in the Supplementary Information.

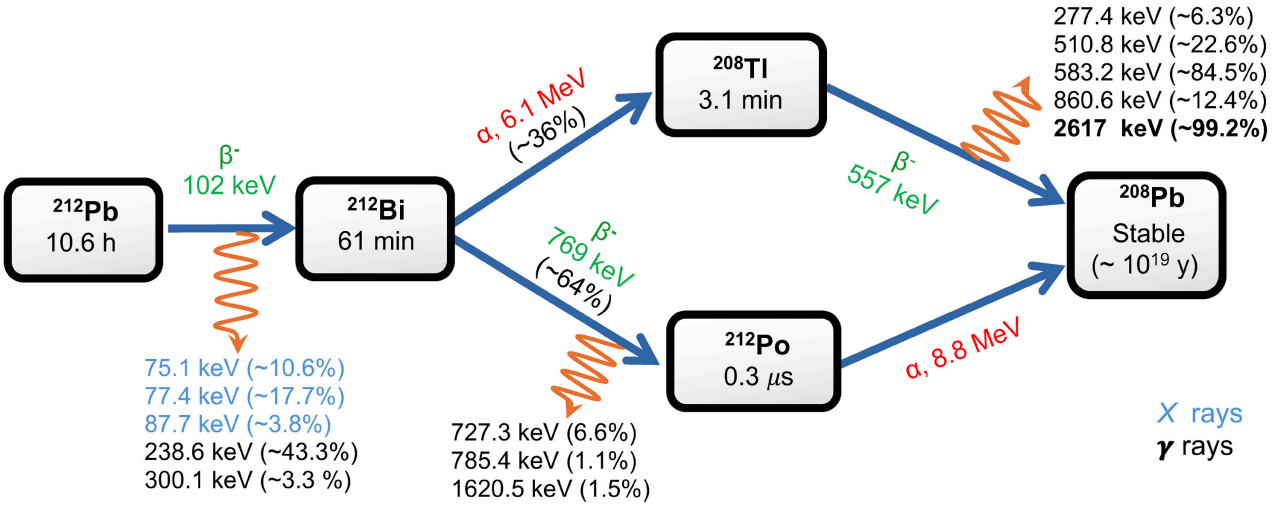


Figure 1. The decay chain of ^{212}Pb (half-life ≈ 10.6 h) terminates in stable ^{208}Pb through a series of α- and β-emitting daughter radionuclides, accompanied by multiple γ-ray emissions spanning approximately 75 keV to 2.7 MeV. The decay scheme is adapted from the National Nuclear Data Center (NNDC), Brookhaven National Laboratory [54].

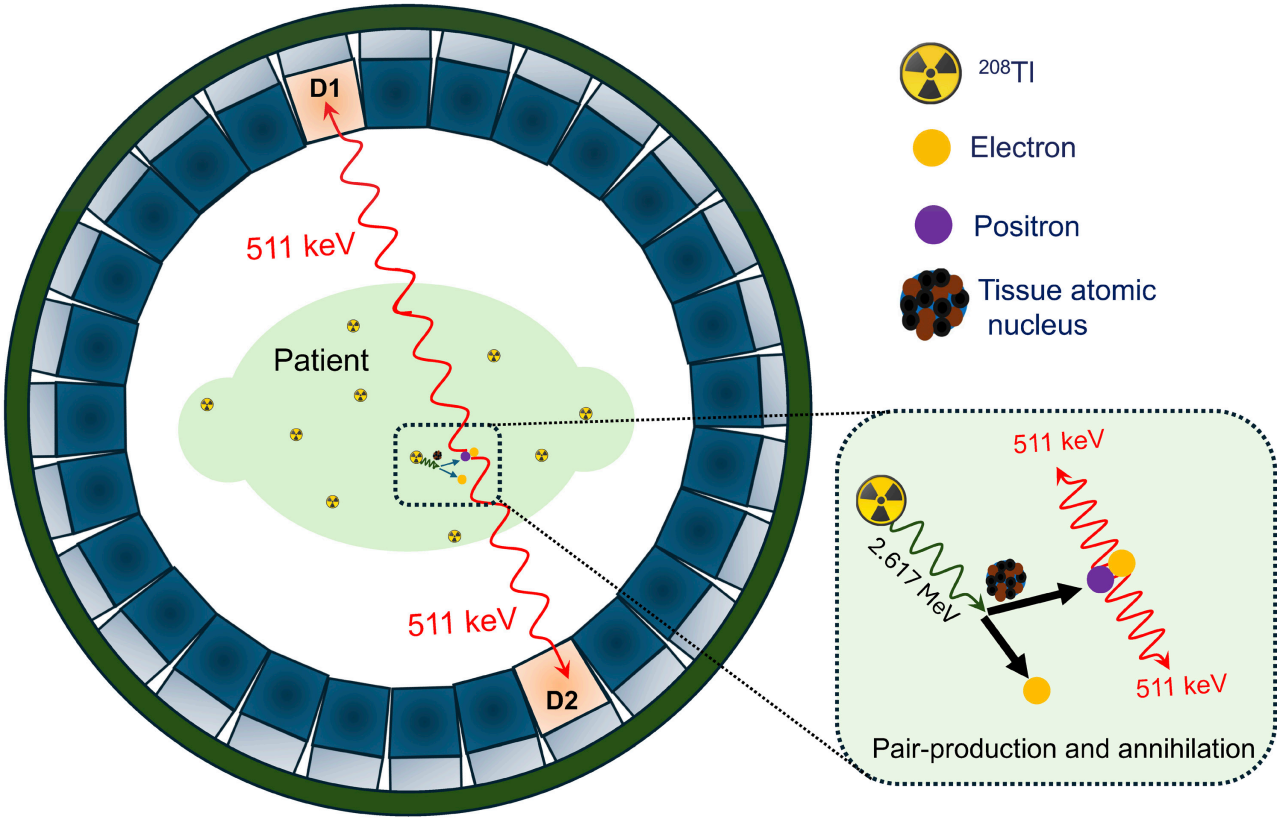


Figure 2. Schematic illustration of pair production (e^+e^-) induced by a 2.617 MeV γ ray, followed by electron positron annihilation producing two 511 keV photons that are detected by a pair of opposite detectors in a PET scanner for tomographic reconstruction.

Figure 3 summarizes the γ- and e^+-range characterization of the 2.617 MeV γ-ray in a homogeneous water cube simulation. The KE distributions of the e^+ and e^- upon pair production were roughly symmetric around $(2.617\ \text{MeV} - 2m_0c^2)/2 = 0.798$ MeV (mean: 0.77 MeV), with an endpoint of 1.56 MeV (**Figure 3A**). Compared to common PET radionuclides, the e^+ energy was between that of ^{18}F (mean: 249.8 keV, endpoint: 633.5 keV) and ^{68}Ga (mean: 836.0 keV, endpoint: 1.899 MeV) [54]. Pair-production events from primary 2.617 MeV γ-rays accounted for 97.9% of the total, while 2.1% originated from secondary or later Compton/ bremsstrahlung photons (see Supplementary Figure S1). All analyses in this study include both contributions unless otherwise noted.

The position of e^+ / e^- production sites $\vec{r_p} = (x_p, y_p, z_p)$ was evaluated in a 1D slice profile of x_p (**Figure 3B**). The profile was normalized and fit to a Lorentzian with exponential background, $f(x) = A(1 + (x/\sigma)^2)^{-1} + B\exp(-C|x|)$, to compute the full width at half-maximum, $\text{FWHM}_p = 0.9$ mm. The spread of x_a from the annihilation point $\vec{r_a}$ was $\text{FWHM}_a = 1.5$ mm (**Figure 3C**). The FWHM of 1D slices of an isotropic point source is sensitive to slice thickness, so this representation was chosen mainly for comparison between the two profiles [65].

The mean range of individual positrons $|\vec{r_{e+}}| = |\vec{r_a} - \vec{r_p}|$ was 2.2 mm, with an endpoint of approximately 7 mm (**Figure 3D**). 2D slice images of production and annihilation events through the cube center (**Figure 3E,F**) illustrate that despite the long range of the 2.617 MeV γ-ray, dispersion in a 3D medium resulted in localized signal near the point source relative to farther events, which appeared as noise.

Positron production and annihilation site distributions were also studied in adipose tissue, lung, water, and bone (**Figure 4**). 1D profiles were generated by summing contributions from each 1-mm slice centered on the Cartesian axes (**Figure 4A,B**). The slice thickness is shaded for visual comparison with the peak width. With higher density ρ and atomic number Z, bone resulted in more localized pair-production and annihilation than materials such as lung tissue (**Figure 4A,B**).

Figure 4C compares the pair production efficiency between materials, defined as the number of production and annihilation events in an arbitrarily selected 1 cm × 1 cm × 1 cm cube centered about the source per primary 2.617 MeV γ-ray photon. As expected, bone also provided the greatest pair production efficiency, over 2.5 times relative to water and adipose tissue, and approximately 13 times

relative to lung tissue. Annihilation efficiencies followed similar trends, with lung tissue exhibiting a larger decrease due to its extended annihilation range. In an infinite medium, and approximately in the full 20 cm × 20 cm × 20 cm cube (Supplementary Figure S2), pair production and annihilation efficiencies are identical, but these data provide an additional heuristic for the signal expected to localize in a small "voxel". Note for absolute interpretation that the ^{208}Tl γ-ray is produced with a branching ratio of approximately 36% per parent ^{212}Pb/^{212}Bi decay (**Figure 1**). Overall, about 97.38% of gamma rays pass through the 1 cm^3 water cube without any interaction, while 2.57% undergo Compton scattering and 0.051% result in pair production, with photoelectric absorption being negligible. Hence, approximately 2% of total interactions result in pair production.

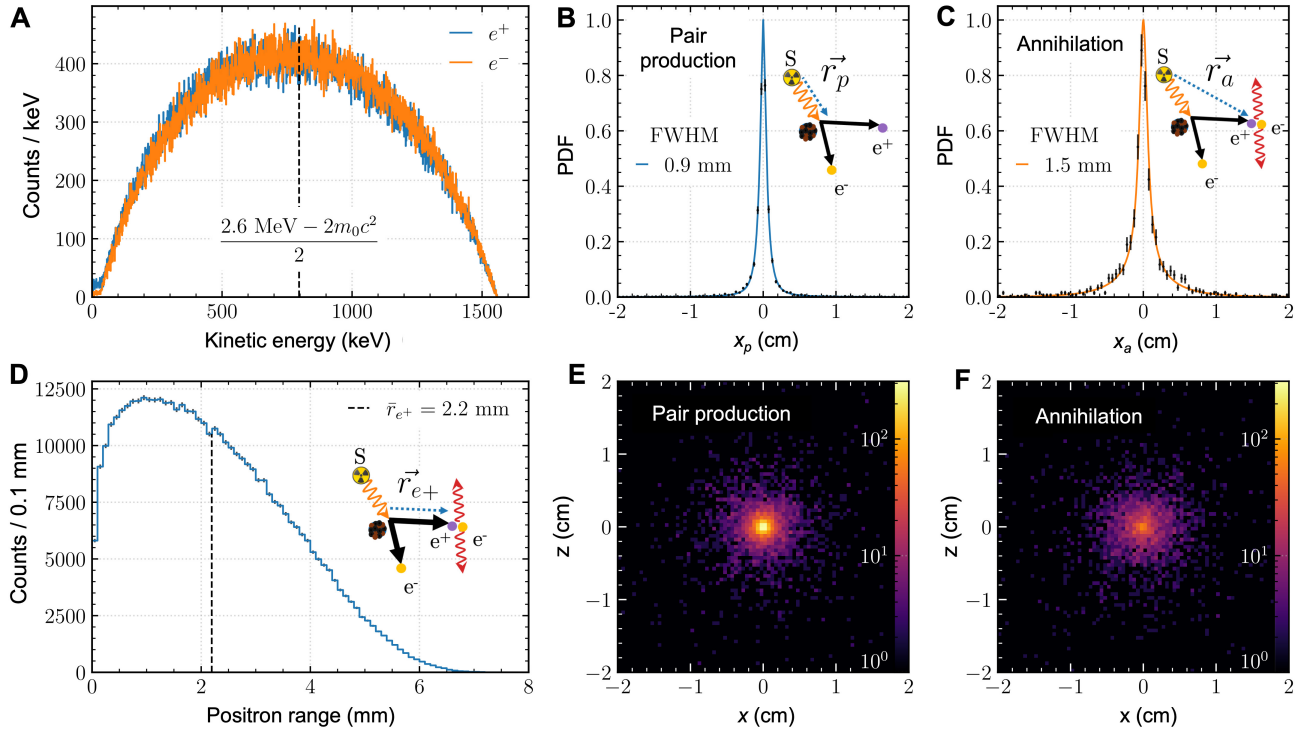


Figure 3. Monte Carlo simulation results: an isotropic point 2.617 MeV γ-ray source was placed at the center of a homogeneous cube water phantom. (A) Kinetic energy distributions of the electron (e^-) and positron (e^+) upon pair production. The distributions are approximately symmetric around (2.617 MeV – $2m_0c^2$/2) = 0.798 MeV. (B) Slice profile of the x-coordinate, x_p, of the vector from the origin to the pair production location, $\vec{r_p}$, with a FWHM of 0.9 mm in a 1 mm slice. (C) Slice profile of the x-coordinate, x_a, of the vector from the origin to the annihilation location, $\vec{r_a}$, with a FWHM of 1.5 mm in a 1 mm slice. (D) Distribution of the positron range, $|\vec{r_{e+}}| = |\vec{r_a} - \vec{r_p}|$. The maximum positron range is approximately 7 mm, with a mean range of 2.2 mm. (E–F) 2D center slices of the pair production and annihilation points, respectively, showing localized source signal.

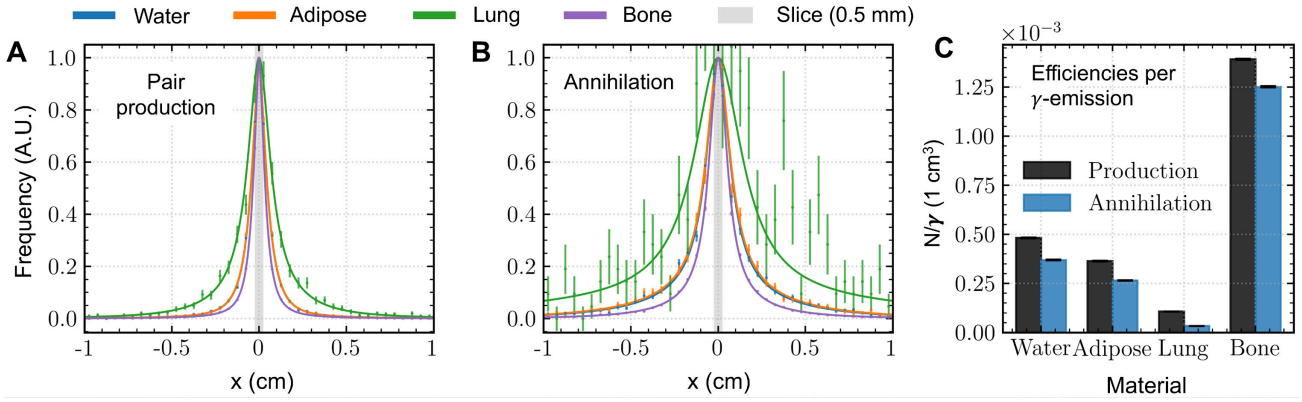


Figure 4. Monte Carlo study of e^+ production and annihilation in homogeneous water, adipose, lung, and bone cubes (20 cm × 20 cm × 20 cm). (A) 1D slice profiles (1 mm) for e^+ production in each material. (B) 1D slice profiles for e^+ annihilation in each material. (C) e^+ production and annihilation efficiencies per primary γ-emission per 1 cm^3 volume centered at the origin. The y-axis has a multiplier of 10^{-3}.

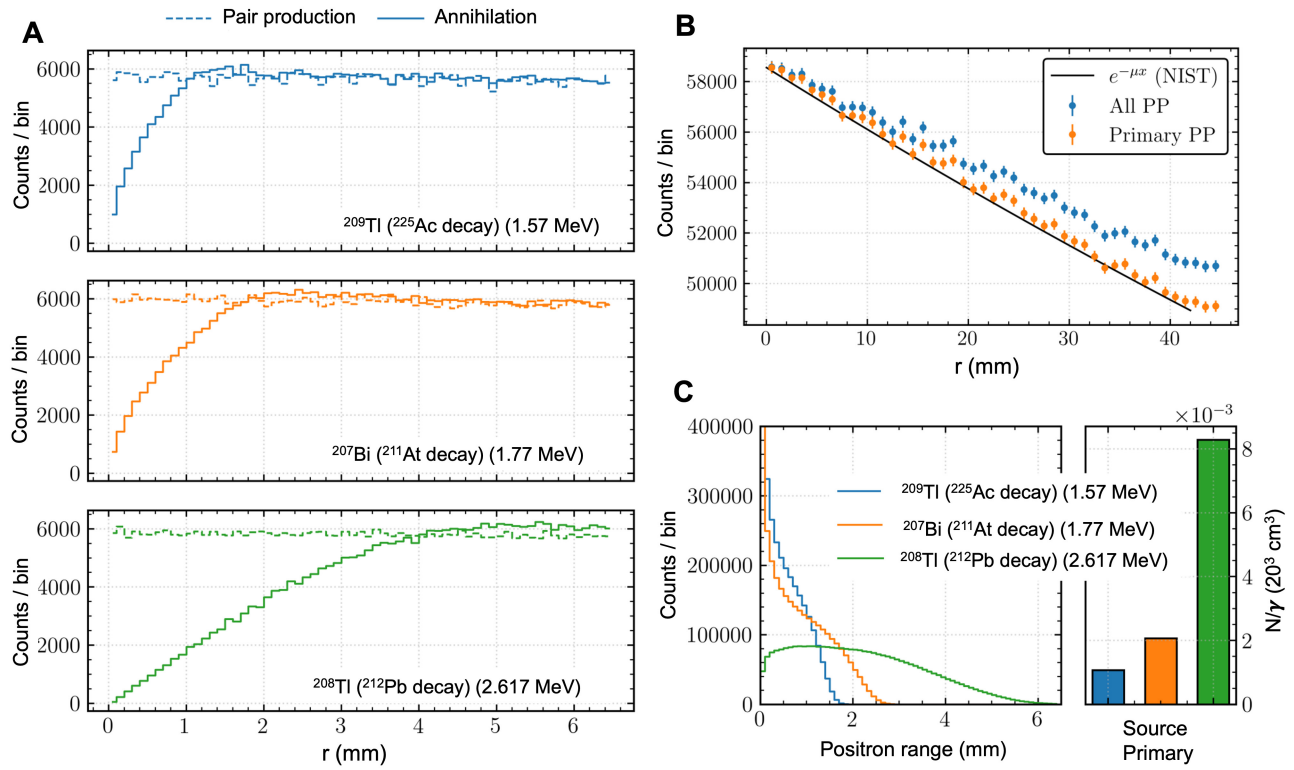


Figure 5. Monte Carlo study of e^+ production and annihilation in water for gamma-emissions in the decay chains of ^{225}Ac, ^{211}At, and ^{212}Pb. (A) Vector magnitude of r_p or r_a results in a 1D illustration of the "build-up" range of the annihilation point with respect to the source. (B) After factoring out the $1/r^2$ radial dispersion and a narrow-beam geometry through selection of primary events, the e^+ production profile of the 2.617 MeV ^{208}Tl gamma-ray is well approximated by exponential attenuation with the NIST linear attenuation coefficient. (C) Simulation results from all three gamma-rays illustrate the trade-off between positron range, where shorter range reduces imaging blur, and pair production efficiency per primary γ-emission per 20^3 cm^3. The γ-axis (N/γ) has a multiplier of 10^{-3}.

Figure 5 illustrates Monte Carlo range simulation results for three gamma-rays found in the decay chains of clinically relevant TAT radionuclides: 1.57 MeV, from ^{209}Tl in the ^{225}Ac series; 1.77 MeV, from ^{207}Bi in the ^{211}At series; and 2.617 MeV, from ^{208}Tl in the ^{212}Pb series. In **Figure 5A**, the vector magnitude of the e^+ production (r_p) and annihilation positions (r_a) are displayed in histogram (0.1 mm bin width), producing 1D illustrations of the annihilation signal build-up and exponential attenuation. By removing the effect of the $1/r^2$ radial dispersion, the e^+ production profile of the 2.617 MeV ^{208}Tl gamma-ray is well approximated by exponential attenuation (**Figure 5B**). When only primary pair-production events are selected, i.e. excluding events resulting from lower-energy Compton or secondary photons, the NIST linear attenuation coefficient for 2.617 MeV provides a good shape approximation [63].

Figure 5C illustrates a trade-off between positron range and pair production efficiency related to the gamma-ray energy. A lower-energy gamma-ray produces shorter-range positrons, but the reduced pair-production cross section significantly reduces the efficiency per gamma-primary. Once branching ratios are included, the efficiency difference widens, with ^{225}Ac, ^{211}At, and ^{212}Pb producing 2.3×10^{-5}, 5.9×10^{-5}, and 3.0×10^{-3} positrons per decay chain parent within the 20 cm × 20 cm × 20 cm cube, respectively.

We also performed simulations of two clinical scale cylindrical phantoms (20 cm diameter and 20 cm length) to investigate the distributions of pair production and annihilation points in realistic geometries. The first phantom contained six cylindrical inserts (20 mm diameter and 38 mm length each) composed of different materials, including water, adipose, lung, brain, bone, and air, embedded within a water-filled background. Total 10^8 2.617 MeV gamma rays were generated isotropically and uniformly within the volume of all inserts. This corresponds to ~0.058 μCi/mL of ^{212}Pb for a 30-min decay in full 4π solid angle. The spatial distributions of pair-production points and annihilation points in the axial planes are shown in **Figure 6A** and **Figure 6B**, respectively. The adipose, bone and brain inserts are clearly distinguishable in both the pair production and annihilation distributions. Although the lung and air inserts appear distinguishable in these distributions, this apparent visibility primarily resulted from the substantially higher pair-production interactions in the surrounding water ($\rho_{water} \approx 1.0$ g/cm^3) than in the lung ($\rho_{lung} \approx 0.26$ g/cm^3) and air ($\rho_{air} \approx 1.2 \times 10^{-3}$ g/cm^3). Therefore, the apparent visualization is not

due to pair-production interactions occurring within the lung and air inserts themselves but instead reflected the surrounding water where the majority of pair-production interactions occurred. These simulation results suggest that bone, brain, adipose tissue, and water equivalent biological samples can be imaged using PPT. However, owing to the low density of lung tissue, signal localization is limited in this region.

The second simulated clinical phantom was designed to reflect the experimentally measured one. It consists of four cylindrical inserts with different diameters (8 mm, 12 mm, 16 mm, and 25 mm) and same length (38 mm), all filled with water with distributed source, to study the effects of insert diameter. The rest of the phantom was filled with water. A total of 10^8 2.617 MeV gamma rays were generated isotropically and uniformly within the volume of these inserts which is equivalent to ~0.128 μCi/mL of ^{212}Pb over a 30-min decay in full 4π solid angle. The spatial distributions of pair production points and annihilation points in the axial planes are shown in **Figure 6C** and **Figure 6D**, respectively. All inserts are clearly resolved down to an insert diameter of 8 mm in both the pair production and annihilation distributions, demonstrating the feasibility of PPT imaging for experimental implementation.

To investigate the applicability of PPT for tumor imaging of different sizes grown in a low-density tissue environment (lung), an additional simulation was also performed with four tumors of 5, 10, 20, and 30 mm diameter embedded within a lung geometry. A total of 10^9 2.617 MeV photons were generated uniformly (equivalent to ~2.21 μCi/mL of ^{212}Pb over a 30-min decay in full 4π solid angle) and isotropically from the tumors according to their respective volume ratios. The resulting pair-production and annihilation-point distributions in the coronal planes are shown in **Figures 7A**,**B**, respectively. All four tumors are visible in the simulated distributions, although the 5-mm tumor appears relatively faint.

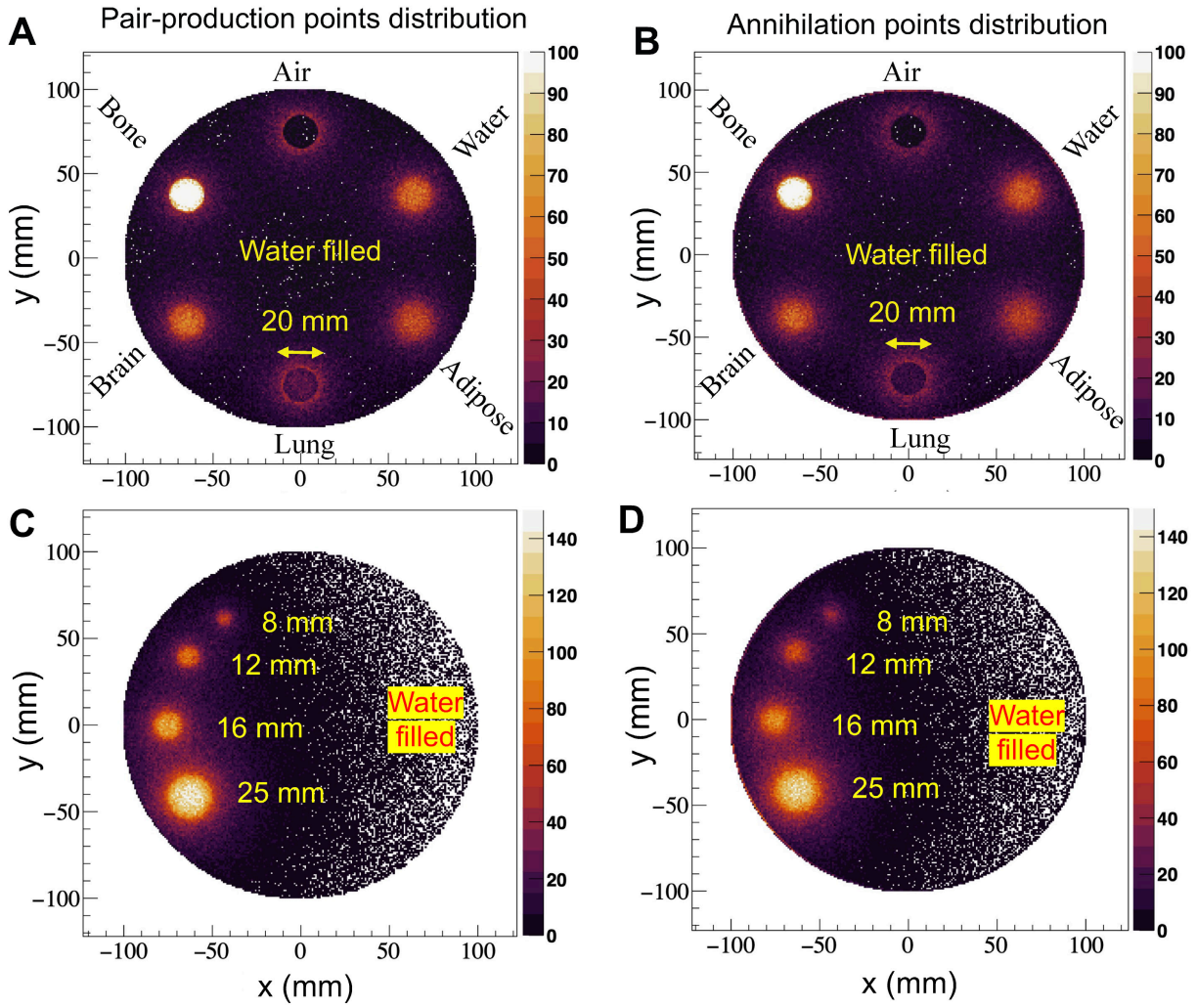


Figure 6. Simulation results of clinical scale cylindrical phantoms for 2.617 MeV gamma rays. (A,B) Pair production and annihilation point distributions in the axial planes for a multi material phantom of 20 cm diameter with six inserts (water, adipose, lung, brain, bone, and air). (C,D) Pair production and annihilation point distributions in the axial planes of second clinical phantom with four inserts of varying diameters showing signal localization.

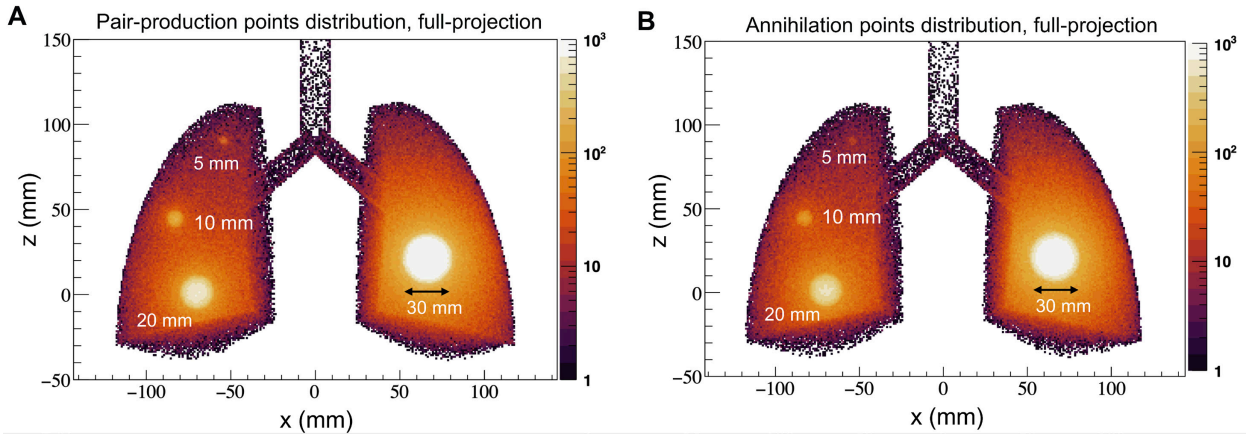


Figure 7. Simulation results of PPT signal localization in a lung phantom containing tumors with diameters of 5, 10, 20, and 30 mm, in the coronal planes. (A) Spatial distribution of pair-production events and (B) corresponding positron annihilation-point distribution following isotropic emission of 2.617 MeV gamma rays from the tumor volumes.

Experimental demonstration of PPT imaging

To demonstrate the feasibility of this new imaging concept, experiments were conducted using two different phantoms: a clinical ACR/Pro-NM PET phantom and a preclinical NU 4-2008 small animal PET phantom. Data were acquired using the Biograph Vision 600 PET/CT (Siemens Healthineers) and the NanoScan microPET/CT (Mediso) scanners for the clinical and preclinical phantoms, respectively. All experiments were conducted at the University of California, San Francisco. For the experiment, ^{212}Pb was eluted in house using a ^{224}Ra/^{212}Pb generator developed by Pacific Northwest National Laboratory (PNNL). Controlled elution ("milking") of ^{212}Pb was performed by passing HCl solution through the generator at a regulated flow rate.

Demonstration with clinical phantom

We filled four cylinders (8, 12, 16, and 25 mm diameters, each 38 mm length) of the ACR/Pro-NM PET phantom with 0.33 μCi/mL of ^{212}Pb (**Figure 8A**). The background volume of the phantom was filled with nonradioactive water. The phantom was scanned using Biograph Vision 600 PET/CT (Siemens Healthineers) for 30 minutes. This PET system incorporates lutetium oxyorthosilicate (LSO) crystals with dimensions of 3.2 mm × 3.2 mm × 20 mm (l × w × t), fully coupled to silicon photomultipliers (SiPMs). Its proprietary detector architecture enables a volumetric resolution of approximately 48 mm^3 while achieving TOF performance of about 214 ps . Pair production tomographic reconstruction of the phantom is shown in **Figure 8B,C** in the axial and coronal planes, using coincident 511 keV events selected from opposing detectors within a coincidence time window defined by the system timing resolution. The acquired list mode data were reconstructed using the vendor-provided iterative reconstruction algorithm incorporating time-of-flight and point-spread-function deblurring as well as CT-based attenuation and scatter corrections in a 440 × 440 × 88 matrix, with 4 iterations and 5 subsets. Post-reconstruction Gaussian filter with 9 mm FWHM was applied to suppress the noise. Line profiles in two directions are also shown in **Figure 8D,E**. The reconstructed image demonstrates the feasibility of PPT imaging using a time-of-flight PET scanner. The three rod inserts are clearly resolved using PPT and are consistent with the simulation results. The reduced intensity of the small rod was attributed to the combined effects of finite spatial resolution and limited counting statistics.

To further evaluate the effect of counting statistics on PPT image quality, an additional clinical phantom experiment was performed using an approximately 1.5 times higher activity concentration and a longer scan time of 180 min, resulting in approximately 10-fold higher event statistics. As shown in **Figure 9**, the increased event statistics substantially improved image quality and enabled visualization of all four active inserts. The smallest rod (8 mm) remained faint, indicating that its reduced visibility is influenced by both limited counting statistics and finite spatial resolution.

For comparison, we have also performed a SPECT scan of the same phantom (filled with 0.33 μCi/mL) with a StarGuide SPECT/CT scanner (GE HealthCare), a commercial digital SPECT/CT system comprising 12 CZT detectors arranged dodecagonally over a 2π angular coverage. The system and its collimation were not specifically optimized for imaging MeV-scale gamma rays. The 79 keV and 239 keV γ rays from the ^{212}Pb emission spectrum were used for SPECT image reconstruction. Triple energy window scatter correction was applied for both reconstructions: the energy window at 79 keV was ± 7% (high scatter window: 88 keV ± 7%; low scatter

window: 67 keV ± 5%), and the energy window at 239 keV was ± 5% (high scatter window: 265 keV ± 5%; low scatter window: 215 keV ± 5%). Images were reconstructed using ordered subsets expectation maximization (OSEM), with 5 iterations and 10 subsets for the 79 keV data, and 8 iterations and 10 subsets for 239 keV data. CT-based attenuation correction was also applied. The final image combined both reconstructed images as summed images. The SPECT image obtained from a 30-minute scan is shown in **Figure 10A,B**. Notably, the larger cylindrical structures, specifically for the 25-mm diameter cylinder, are clearly visible and show comparable features to those observed in the pair production tomography images. However, the remaining three rods are less clearly resolved at the given activity.

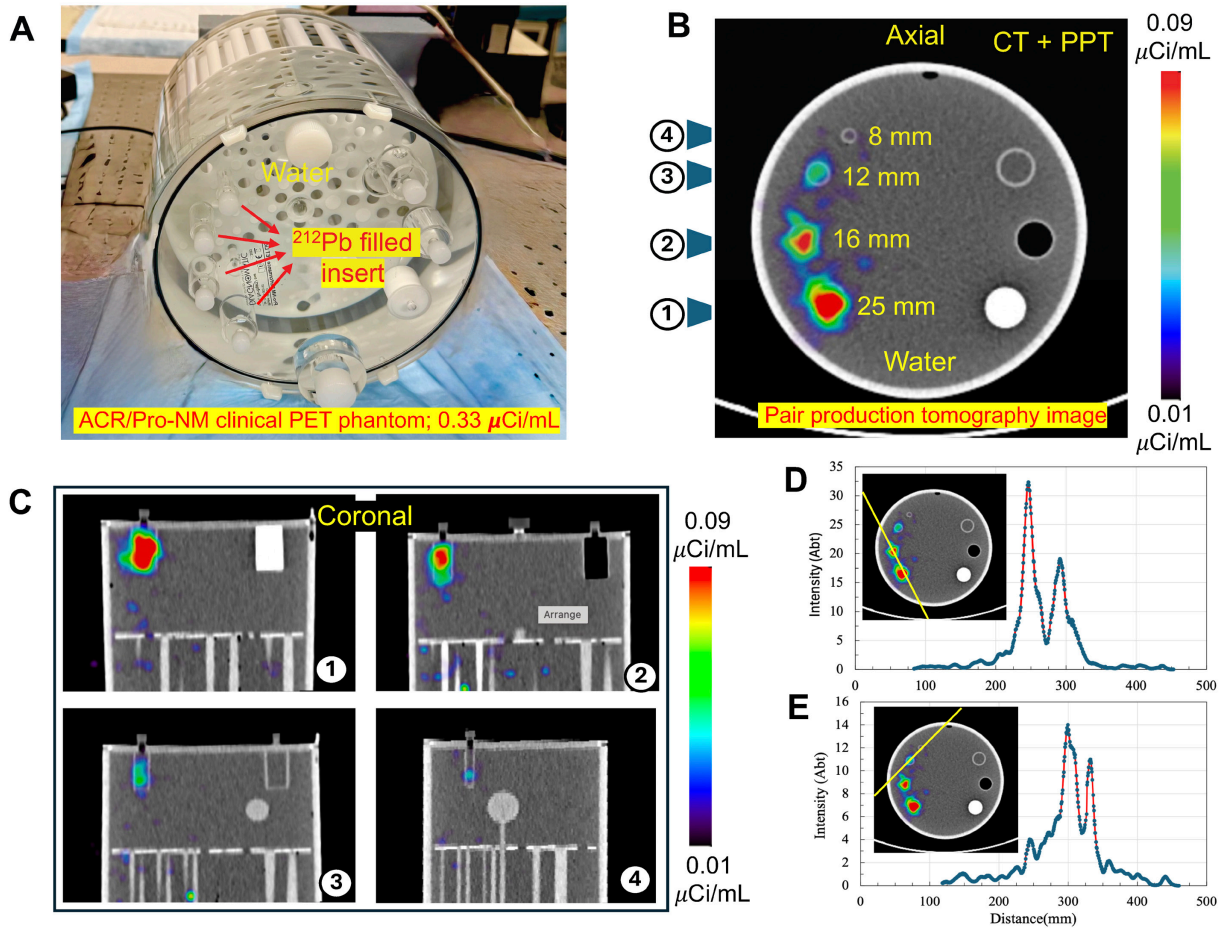


Figure 8. Experimental PPT imaging results of the ACR/Pro-NM clinical PET phantom filled with ^{212}Pb solution (0.33 μCi/mL) in four cylindrical inserts. (A) The phantom was scanned using Biograph Vision 600 PET/CT (Siemens Healthineers) for 30 minutes. (B) Pair production tomography (PPT) image reconstructed from coincident 511 keV gammas, projection on axial plane. (C) The projection images of four inserts on coronal plane. (D,E) The line profiles of the pair production images.

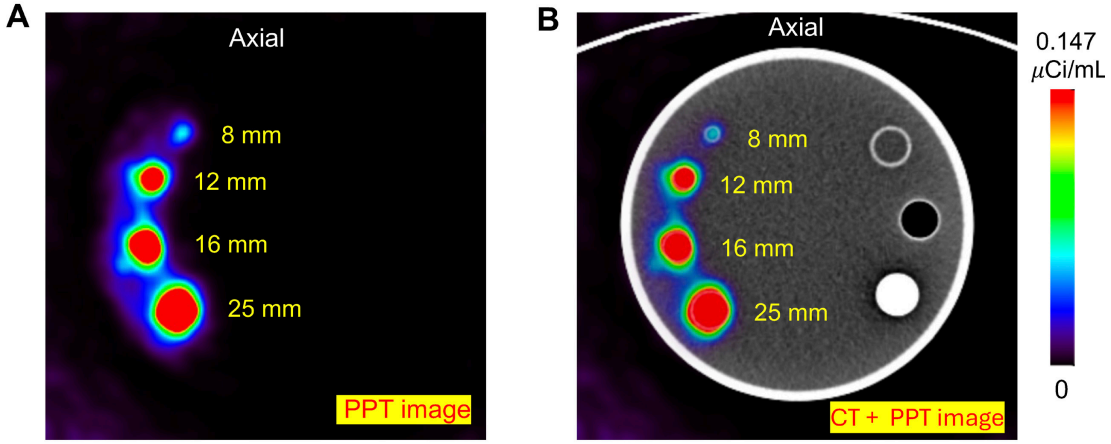


Figure 9. Axial slice of (A) experimental PPT image of the ACR/Pro-NM clinical PET phantom containing four cylindrical inserts filled with ^{212}Pb solution (0.50 μCi/mL), acquired over 180 min. (B) PPT image superimposed on the CT image.

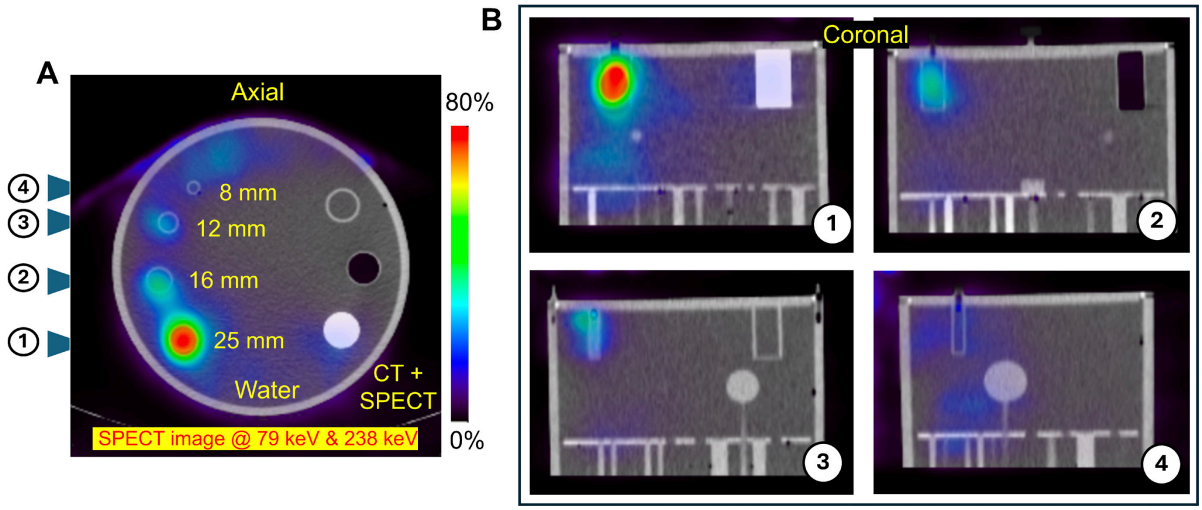


Figure 10. (A) Fused CT and SPECT image of the clinical phantom with four cylindrical inserts filled with ^{212}Pb solution (0.33 μCi/mL), acquired over 30 minutes using the StarGuide SPECT/CT system with 79 keV and 239 keV energy windows in the axial plane. (B) Corresponding projection views of four inserts in the coronal plane.

Demonstration with small cylindrical phantom

We performed an additional experiment using a small cylindrical phantom (NU 4-2008 PET phantom, shown in **Figure 11A**). The phantom contains two internal cylindrical inserts (8 mm diameter and 14 mm length), one filled with non-radioactive water and the other with air. The remaining volume of the phantom was uniformly filled with water containing ~5.365 MBq (0.145 mCi) of ^{212}Pb dissolved in 20.9 mL of water. The phantom was first scanned using the non-TOF NanoScan microPET/CT (Mediso) system. This PET system is equipped with a 16 cm gantry bore and utilizes LYSO crystal elements with dimensions of 1.12 × 1.12 × 13 mm^3. Combined with its proprietary reconstruction algorithm, the system achieves a PET spatial resolution of approximately 0.7 mm. The integrated CT component provides high resolution anatomical imaging with a spatial resolution of up to 30 μm. The phantom was scanned for 30 minutes, and pair production image reconstruction was performed using the vendor-provided 3D iterative reconstruction algorithm with 40 iterations and 1 subset (i.e., maximum likelihood expectation maximization, not OSEM). The reconstructed CT and combined CT and PET images are shown in **Figure 11B-D** in three orthogonal planes. As expected, negligible annihilation events are observed within the air-filled cylindrical insert.

In contrast, the insert containing non-radioactive water shows a distribution of annihilation events arising from the passage of 2.617 MeV gamma rays through this region, which produce electron positron pairs and subsequent annihilation events. This NanoScan experiment shows that PPT coincidence events generated by the 2.617 MeV gamma emission can be reconstructed using a non-TOF PET system. However, the limited contrast of the non-radioactive water insert indicates reduced image localization under these conditions. As the NanoScan microPET system does not support TOF capability, the reconstructed images show reduced clarity and exhibit signal within the non-radioactive water region, indicating that time of flight will significantly reduce background in the reconstructed images as described in the next subsection.

We also performed imaging of the same phantom using a small animal SPECT scanner, the VETor4CT microSPECT/CT (MILabs), with energy window selection of 79 keV and 239 keV, ±10% for both energy peaks. The vendor-provided automatic CT-based attenuation and triple-energy window scatter correction were applied to SPECT reconstruction. We used the HE-GP-RM that has 156 pinholes arranged as 4-pinholes clustered into one combined hole to handle high-energy photons and provides high-sensitivity (2%) that is essential to image radionuclides like ^{212}Pb. The reconstructed SPECT image, overlaid with the CT image, is shown in **Figure 12**. The two internal cylindrical inserts are clearly resolved, with no detected activity within these regions, as expected.

Effect of time-of-flight (TOF) reconstruction on PPT image quality

To directly evaluate the effect of TOF information on PPT reconstruction, the same Biograph Vision 600 PET/CT dataset with 10-fold higher event statistics was reconstructed with TOF information enabled and disabled using the vendor-provided offline reconstruction software. All other conditions, including scanner, phantom, activity concentration,

and acquisition data were identical between the two reconstructions. As shown in **Figure 13**, the TOF-enabled reconstruction exhibited improved image contrast and reduced background compared with the TOF-disabled reconstruction.

As an additional comparison, the NU 4-2008 phantom was also imaged using the TOF Biograph Vision 600 PET/CT (in Supplementary Material). As the two scanner systems differ in spatial resolution, sensitivity, detector geometry, and reconstruction, this comparison was considered supportive rather than a direct assessment of TOF alone. ROI analysis showed a higher radioactive-to-nonradioactive water ratio for the TOF Biograph Vision 600 image than for the non-TOF NanoScan image (1.9 vs. 1.1), while the radioactive-to-air ratios were 5.0 and 3.37, respectively. A brief description and discussion of this result is given in the Supplementary Material.

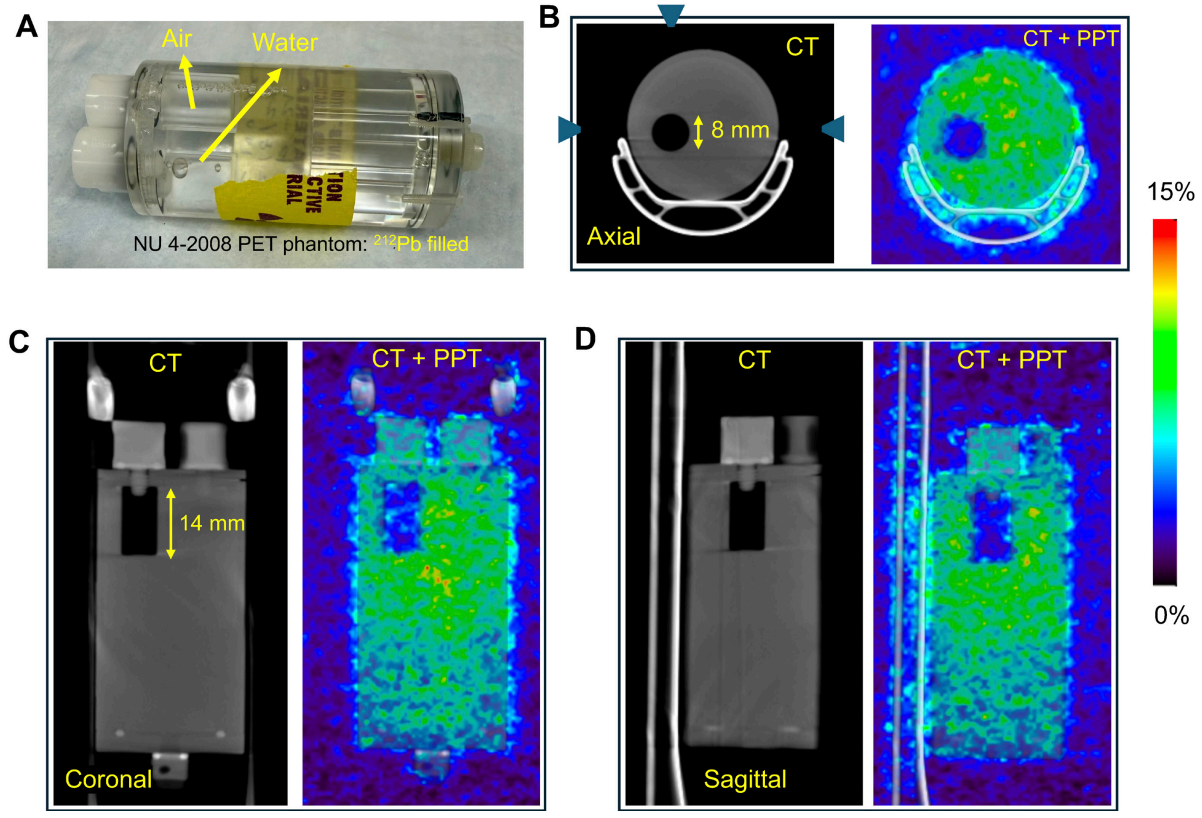


Figure 11. Imaging results of the NU 4-2008 small animal PET phantom filled with ^{212}Pb solution (0.145 mCi in 20.9 mL), containing two internal cylindrical inserts (water and air). (A) Photograph of the phantom. (B-D) Fused CT and PPT image reconstructed from 511 keV coincidence events using the NanoScan microPET/CT system. Annihilation events are observed within the radioactive water regions, including the water filled insert and plastic material while negligible activity is seen in the air-filled insert.

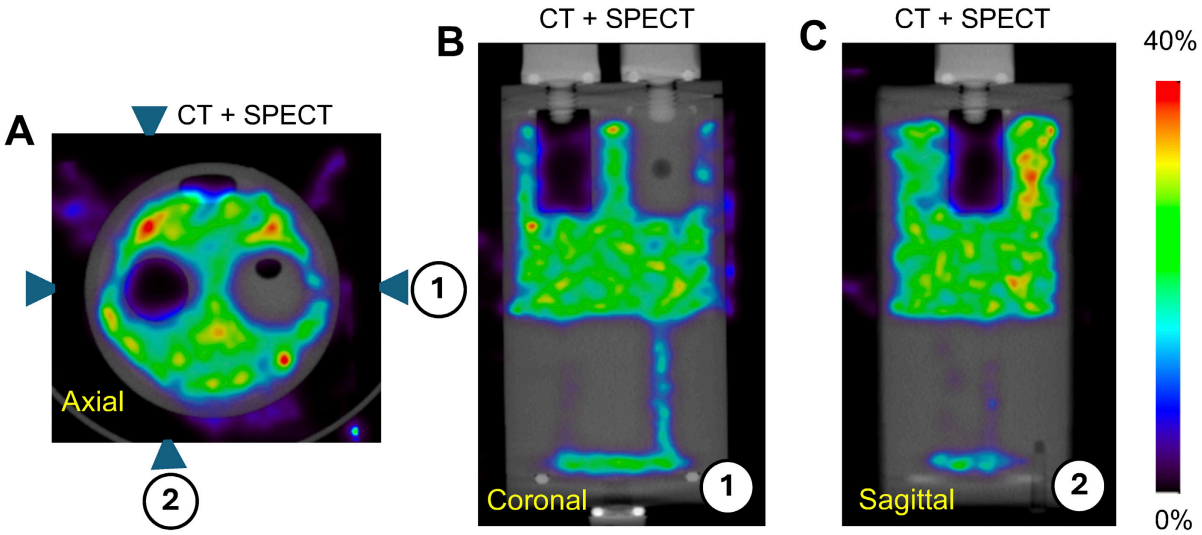


Figure 12. (A-C) SPECT image overlaid with CT acquired using the VETor4CT microSPECT/CT system with 79 keV and 239 keV energy windows. Two inserts, one air filled and one containing non-radioactive water, are clearly distinguished from the rest volume radioactive water region.

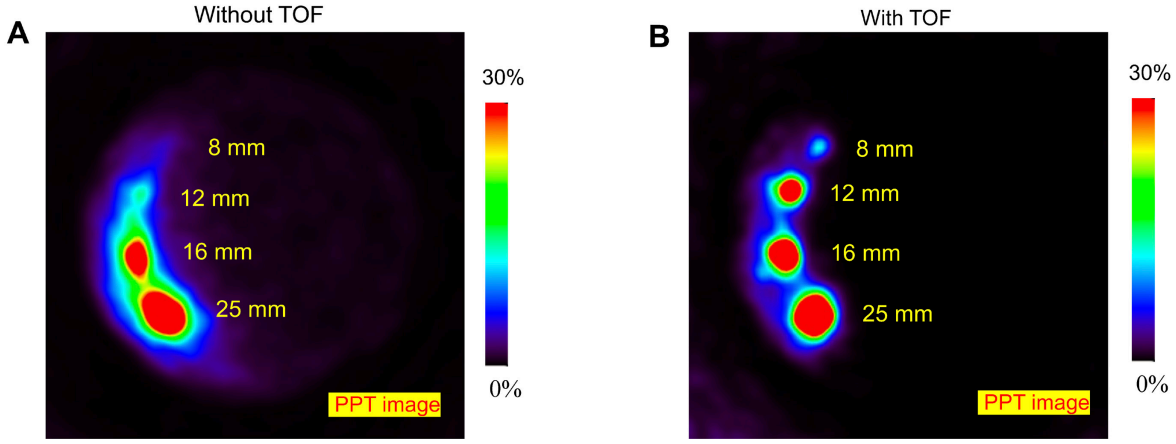


Figure 13. Reconstructed PPT images (in axial plane) using the Biograph Vision 600 PET/CT of same dataset of identical phantom, activity concentration, and acquisition conditions: (A) TOF-disabled reconstruction and (B) TOF-enabled reconstruction. The comparison demonstrates improved PPT image quality with incorporation of TOF information.

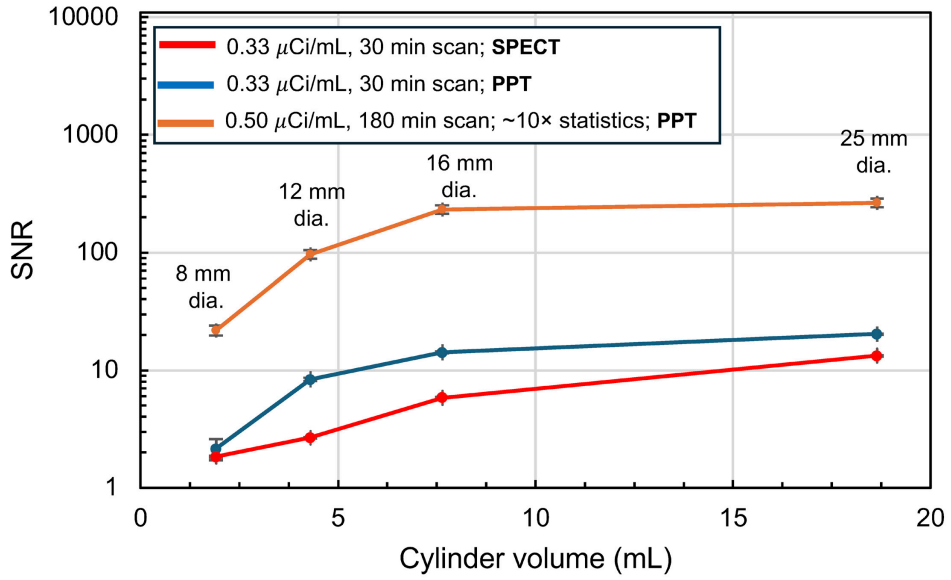


Figure 14. ROI-based SNR as a function of insert volume for the two PPT measurements with different event statistics and the corresponding CZT-SPECT measurement.

Quantitative assessment of PPT image quality and activity recovery

The ROI-based signal-to-noise ratio (SNR) of PPT and SPECT images of ACR/Pro-NM PET phantom have been obtained and shown in **Figure 14**. These results illustrate detectability increasing as a function of insert volume. With approximately 10-fold higher event statistics of PPT images, the SNR increased markedly for all inserts, including the 8-mm rod, demonstrating substantially improved contrast at higher statistics.

Quantitative analysis was also performed by defining small regions of interest (ROIs) within each insert to determine the activity recovery. This analysis of the PPT images showed a clear dependence of activity recovery on rod size as shown in **Figure 15**. The 25-mm rod of 10-fold statistics measurement was used as the reference measured known activity. The activity recovery decreased to 90.1 ± 1.5%, 55.7 ± 1.3%, and 11.3 ± 0.3% for the 16-, 12-, and 8-mm rods, respectively. Compared with the lower-statistics measurement, improved recovery was observed across the smaller rods, indicating that the quantitative performance of PPT is influenced by both object size and the available event statistics.

Discussion

This study demonstrates the experimental feasibility of pair production tomography for imaging the 2.617 MeV gamma-ray emission in the ^{212}Pb decay chain. Monte Carlo simulation results show that this signal can be localized sufficiently for PET imaging, despite the long interaction range of MeV gamma rays and the inherently low probability of pair production. The main finding of this work is that PPT expands radionuclide imaging beyond the conventional energy range of current clinical imaging without direct

positron emission by radionuclide. While SPECT is highly effective for single-photon imaging at sub-MeV energies, its performance degrades at higher photon energies because of reduced detection efficiency, increased scatter, and collimator penetration. By contrast, PET enables highly sensitive coincidence detection and quantitative reconstruction but is generally restricted to radionuclides that undergo direct positron emission.

PPT addresses this limitation by transforming high energy gamma emission into a coincidence signal detectable with PET. In this context, the method goes beyond the existing imaging approaches and establishes a distinct framework for probing high energy emissions that are difficult to visualize with conventional medical scanners. This strategy is particularly relevant for current and emerging therapeutic radionuclides used in particle therapy that emit gamma rays in the MeV range, such as ^{212}Pb based targeted alpha therapy. Although ^{212}Pb is the administered radionuclide, therapeutic dose deposition is driven by its alpha emitting daughter products. Imaging of the parent radionuclide alone therefore may not accurately reflect the spatial distribution of these alpha emitting components. By exploiting the 2.617 MeV gamma emission from ^{208}Tl, PPT provides a means to localize a therapeutically relevant daughter pathway within the decay chain.

Our simulation results clarify why such imaging is possible. Owing to its initial kinetic energy (**Figure 3A**), the positron travels an average distance of approximately 2.2 mm before annihilating with an electron (**Figure 3D**), a range that remains compatible with PET imaging. Although the 2.617 MeV gamma ray exhibits a long attenuation length (~23.4 cm) in tissue equivalent media, the isotropic geometric dispersion ($1/r^2$) concentrates the detected signal near the source region (**Figure 3B-F**). In water, the annihilation distribution remains localized to within ~ 2 mm, while the degree of localization varies systematically with material composition and density. This uncertainty is further propagated through the intrinsic PET resolution during PPT imaging. High density media such as bone, brain, adipose, and water preserve the signal more effectively, whereas lung tissue exhibits less localization owing to its lower density and extended annihilation range (**Figure 6B**). These findings are important for interpreting PPT images in heterogeneous anatomical environments and indicate that tissue composition will influence both sensitivity and spatial resolution. The additional simulation results (**Figure 7**) also indicate that PPT can retain tumor-associated spatial information even for small lesions embedded in a low-density lung environment. However, the visibility decreases with decreasing tumor size, as observed for the 5-mm tumor. In practical applications, the detectability of such small lesions will also depend on the available activity, counting statistics, surrounding tissue heterogeneity, and detector sensitivity. Therefore, further studies using realistic anatomical geometries and activity distributions will be necessary to establish the practical detection limits of PPT.

The simulation results (**Figure 5**) of three MeV-scale gamma-rays found in the decay chains of clinically relevant TAT radionuclides indicate that gamma-ray energy and branching ratio are relevant to a trade-off in PPT between positron range and pair-production efficiency. Among the radionuclides considered, the 2.617 MeV emission in the ^{212}Pb decay chain provides the highest simulated pair-production yield, while lower-energy emissions offer shorter positron ranges but reduced efficiency.

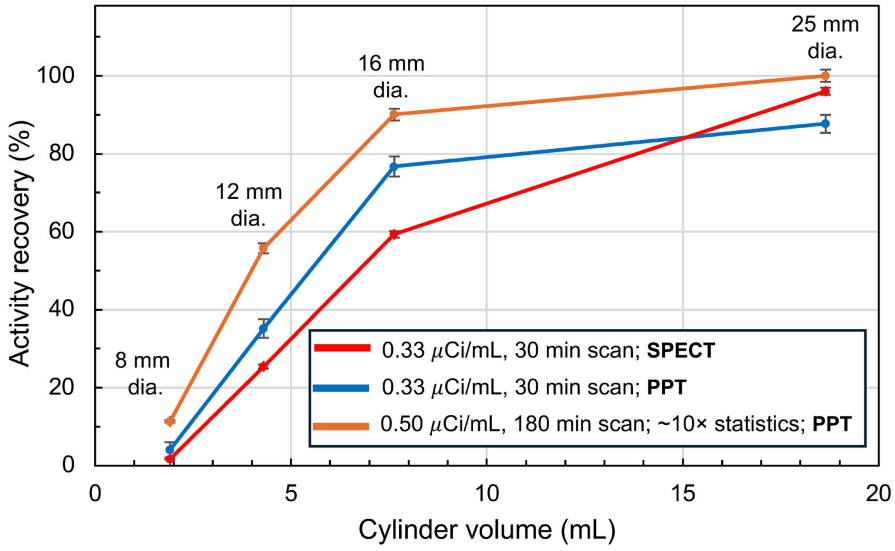


Figure 15. Activity recovery for the 8-, 12-, 16-, and 25-mm rods obtained from the ROI based analysis of two PPT measurements with different event statistics.

The experimental phantom studies further validate the PPT concept. In the clinical phantom, PPT performed on a modern TOF PET system resolved the larger rods (**Figures 8** and **9**) and produced image features consistent with the simulated distributions. In the preclinical small phantom, pair production imaging was observed using a non-TOF microPET system (**Figure 11**), thereby confirming experimentally that the signal can be reconstructed using PPT. However, the reduced clarity and elevated background observed in the non-radioactive water insert in the absence of TOF capability indicate that timing information plays a central role in practical imaging performance. The controlled TOF-on versus TOF-off reconstruction provides (**Figure 13**) direct experimental evidence that incorporation of TOF information improves PPT image quality under otherwise identical conditions. These findings show that PPT can be implemented on existing PET systems, while identifying TOF capability as an important factor for enhancing localization. The comparison with SPECT is also informative. In the clinical phantom, SPECT clearly visualized the largest insert but showed reduced visibility for the smaller rods under the low activity conditions examined here (0.33 μCi/mL) (**Figure 10**), owing to increased septal penetration and scatter background from high energy gamma emissions and require further optimization and correction. This SPECT comparison reflects the specific acquisition and reconstruction protocol used in this study. High-energy-optimized collimation and improved scatter, down-scatter, and septal-penetration corrections could potentially improve SPECT performance. Nevertheless, physical collimation imposes an inherent sensitivity-spatial-resolution trade-off, whereas PPT uses coincidence detection and TOF localization without physical collimation, which may be advantageous under low-count conditions. PPT also provides complementary information about the ^{208}Tl daughter distribution. For imaging ^{212}Pb and its progeny, PPT provides daughter-sensitive information that could more closely reflect the spatial distribution of therapeutic α-emission dose than imaging the parent ^{212}Pb distribution alone. Hence, the present results suggest that PPT may complement, rather than replace, existing SPECT based approaches for selected theranostic radionuclides with suitable high energy (MeV range) emissions.

Our PPT study at 12 kBq/mL (0.33 μCi/mL) with a 30 min acquisition lies within a clinically relevant activity range for ^{212}Pb PSMA imaging. In a first-in-human microdose study of ^{212}Pb-AB001, a lymph node metastasis was visualized on SPECT/CT. Its ^{212}Pb activity concentration was estimated to be approximately 5.4 kBq/mL by extrapolating from baseline ^{18}F-PSMA-1007 PET uptake, using the lesion SUV_{mean}, patient body weight, and decay-corrected administered ^{212}Pb activity, rather than by direct SPECT quantification. Separate phantom measurements characterized SPECT image contrast at activity concentrations down to 2 kBq/mL [47]. In addition, therapeutic imaging with ^{212}Pb ADVC001 using SPECT/CT with energy windows at 238.6 keV and 75-91 keV, following administration of 60 MBq, demonstrated tumor uptake consistent with PSMA PET, despite the challenging imaging conditions associated with ^{212}Pb, including scatter from high energy daughter emissions [46]. These comparisons indicate that PPT sensitivity at 12 kBq/mL lies within the range of activity concentrations observed in human ^{212}Pb PSMA studies and may support clinically meaningful post therapy imaging. In addition, TOF total body PET systems are expected to substantially enhance sensitivity for PPT. The improved visualization (**Figure 9**) obtained with approximately 10-fold higher event statistics suggests that increased PET system sensitivity could substantially enhance PPT image quality and small-lesion detectability. This finding motivates for the future implementation of long-axial-field-of-view, high-sensitivity PET systems for PPT imaging without increasing administered therapeutic activity. However, the persistent reduced visibility of the smallest insert indicates that finite spatial resolution remains an important limiting factor.

The improvement in SNR values with increased event statistics (**Figure 14**) indicates that the small-structure detectability in PPT image is count-dependent in addition to being limited by spatial resolution and partial-volume effects. The improved SNR of the 8- and 12-mm inserts at higher statistics further supports the potential benefit of higher-sensitivity TOF PET systems for PPT. However, the PPT and CZT-SPECT SNR values should be regarded primarily as a contrast comparison rather than a direct performance comparison, because the two modalities use different gamma-ray energies and fundamentally different detection mechanisms. The insert size dependent activity recovery (**Figure 15**) indicates that quantitative PPT imaging is influenced by partial-volume effects and by event statistics, particularly for smaller structures. Importantly, the reported recovery values are relative values normalized to the 25-mm rod in the higher-statistics measurement. As the relative recovery curve does not reach a plateau at the largest insert, absolute activity recovery may be lower than the relative values reported here. Establishing absolute quantitative PPT will therefore require dedicated future measurements over a range of

activity concentrations, count levels, and object sizes, together with appropriate partial-volume and reconstruction corrections.

In the context of future *in vivo* applications, therapeutic α emissions arise from ^{212}Bi and ^{212}Po rather than ^{212}Pb. Partial release and redistribution of ^{212}Bi can therefore separate α-emission sites from the parent distribution, providing an important motivation for daughter-sensitive imaging. The extremely short half-life of ^{212}Po means that its α emission occurs essentially at the preceding ^{212}Bi β-decay site. In the approximately 36% α branch, ^{208}Tl is produced at the ^{212}Bi α-decay site. Its approximately 3.1-min half-life, compared with 60.5 min for ^{212}Bi, provides a rationale for investigating PPT as a potentially more representative marker of daughter-associated α-emission sites than parent imaging alone, provided subsequent ^{208}Tl transport is limited. Combining PPT with direct ^{212}Pb SPECT or imaging of the corresponding ^{203}Pb-labeled radiopharmaceutical could provide complementary information on parent delivery and daughter distribution for future dosimetry.

Regarding the current limitations and opportunities for future development, first, pair production remains a relatively infrequent interaction channel at 2.617 MeV, and sensitivity is therefore constrained by the gamma-ray branching ratio, interaction probability, scanner geometry, and counting statistics. Thus, scanner sensitivity and timing performance are important determinants of PPT image quality. An additional background contribution may arise from 2.617-MeV photons escaping the phantom and undergoing pair production within scanner hardware. Because the resulting annihilation photons have the same 511-keV energy as object-generated events, energy gating/windowing alone cannot distinguish these contributions. TOF localization substantially reduced nonlocal background (**Figure 13**), although hardware-generated events may not be completely rejected. Their relative contribution could not be quantified from the present measurements and will require dedicated Monte Carlo modeling incorporating the full scanner geometry and material composition. Second, quantitative PPT reconstruction and image interpretation may be influenced by the spatial distribution of pair-production and annihilation events, which also depends on tissue composition and photon transport. An additional consideration for reconstruction and quantitative PPT is that conventional PET attenuation and scatter corrections do not fully model the underlying PPT physics. Standard 511-keV attenuation correction remains applicable to the annihilation photons traveling from the annihilation site to the detectors but does not account for transport of the primary 2.617-MeV photon before pair production. Similarly, conventional PET scatter correction does not explicitly account for scattering of the primary high-energy photon prior to pair production. These effects may slightly introduce spatially and material-dependent quantitative bias. Future reconstruction and quantitative PPT will therefore require a dedicated forward model incorporating MeV-scale photon attenuation and scattering, material-dependent pair-production probability, positron transport, 511-keV photon attenuation and scatter, and detector/TOF response, potentially through Monte Carlo-based system modeling and dedicated iterative reconstruction. Third, absolute quantitative recovery has not yet been established for PPT. The observed activity recovery differed between measurements acquired under different activity-concentration and count-statistics conditions. As these factors were not independently varied, their respective contributions cannot be determined. Systematic calibration across independently controlled activity concentrations and count levels will therefore be required for absolute quantitative PPT. Finally, the potential dosimetric benefit requires *in vivo* validation, particularly assessment of ^{208}Tl redistribution following ^{212}Bi α decay. Absorbed-dose estimation will additionally require validated absolute activity calibration, serial imaging, and modeling of decay branching, daughter kinetics, the PPT spatial response, and energy deposition. These relationships are beyond the scope of this experimental study.

Biological transport of daughter radionuclides may cause PPT localization to differ from parent ^{212}Pb targeting. The recoil associated with ^{212}Bi α decay breaks the molecular binding of ^{208}Tl, while its subsequent movement is governed by cellular and tissue retention. Published ^{201}Tl studies [66] indicate a cellular washout half-time of ~15 min in prostate and breast cancer cells following medium replacement, while only 5–8% of intravenously administered activity remained in human blood at 5 min [67]. Because these observations represent distinct biological compartments, they cannot be directly extrapolated to recoil-released ^{208}Tl. Its 3.05-min half-life promotes decay before slower tissue clearance, although rapid redistribution of a released fraction remains possible. Thus, loss from the target and uptake in other tissues may influence PPT contrast and localization. PPT maps ^{208}Tl decay sites, whose spatial relationship to preceding α-emission sites is determined by daughter retention. The redistribution of upstream ^{212}Bi may additionally increase their separation from parent targeting. Future *in vivo*

quantitative assessment will require coupled parent-daughter kinetic modeling validated by serial isotope-resolved biodistribution measurements incorporating decay and ingrowth corrections.

These limitations outline a pathway for further development, with improvements in timing resolution, detector technology, total body PET sensitivity, event classification, and model-based reconstruction expected to enhance overall performance. Scanner designs optimized for high sensitivity coincidence imaging may be particularly advantageous for PPT, especially in the low activity regime relevant to TAT. Beyond ^{212}Pb, this conceptual framework may be extended to other novel radionuclides that emit MeV-scale gamma rays. More broadly, these results suggest that the high energy photons of theranostic decay spectra, often regarded primarily as a source of image degradation, can instead be harnessed for tomographic imaging.

Conclusion

We present the experimental demonstration of pair production tomography for non-positron emitting radionuclide based on the 2.617 MeV gamma-ray imaging in the ^{212}Pb decay chain. Simulation and experimental studies show that pair production and subsequent annihilation events can be localized and reconstructed tomographically, with imaging performance enhanced by time-of-flight PET capability. These results establish PPT as a feasible approach for imaging theranostic radionuclides of non-positron emitter daughters which emit MeV-range gamma rays. Our study suggests a pathway for localizing therapeutically relevant daughter distributions in ^{212}Pb based targeted alpha therapy. These results further motivate the development of novel TAT-based radiopharmaceuticals for theranostics applications by demonstrating the potential for high energy imaging using PPT. With continued advances in detector technology, timing performance, and quantitative reconstruction methods, PPT may broaden the capabilities of nuclear medicine imaging and support improved validation of emerging theranostics treatments.

Supplementary Material

Supplementary data, figures and table.
https://www.thno.org/v17p0716s1.pdf

Acknowledgments

The authors thank Anil Bidkar for helping elution of ^{212}Pb from ^{224}Ra/^{212}Pb generator manufactured at Pacific Northwest National Laboratory (PNNL), procured through the National Isotope Development Center. The authors thank Matthew J. O'Hara at PNNL for his generous support to produce this generator. The authors declare no other known conflicts of interest, financial or personal, that could have influenced the work reported in this article. We also acknowledge the assistance of Grammarly and ChatGPT (OpenAI) for language polishing, grammar correction, and improving the readability of the manuscript. All AI-assisted polished sentences were carefully reviewed and verified by the authors. No AI tools were used for study design, simulation modeling, code, data collection, data analysis, image generation, conceptualization, or interpretation of the results.

Funding

This work was supported by the National Cancer Institute (NCI) grant R01CA279203 and the National Institute of Biomedical Imaging and Bioengineering (NIBIB) grant R01EB032324.

Data, code and materials availability

The experimental and simulation data that support the findings of this study are available from the corresponding author upon reasonable request.

Author contributions

Y.S. conceived the idea of PPT imaging of this project and led the project. B.D., Y.S., and J.C. designed and performed the experiments. B.D. and Y.S. performed the data analysis. R.P. and B.D. conducted the Monte Carlo GATE/GEANT4 simulations. All authors, B.D., R.P., Y.S., and J.C. contributed to the interpretation of the experimental and simulation results, the discussion, and the preparation of the manuscript.

Competing interests

The authors have declared that no competing interest exists.

References

1. Weber WA, Czernin J, Anderson CJ, Badawi RD, Barthel H, Bengel F, et al. The future of nuclear medicine, molecular imaging, and theranostics. J Nucl Med. 2020; 61 (Suppl 2): 263S-272S.
2. Schwenck J, Sonanini D, Cotton JM, Rammensee HG, la Fougère C, Zender L, et al. Advances in PET imaging of cancer. Nat Rev Cancer. 2023; 23: 474-490.
3. Weissleder R, Pittet MJ. Imaging in the era of molecular oncology. Nature. 2008; 452: 580-589.
4. Gambhir SS. Molecular imaging of cancer with positron emission tomography. Nat Rev Cancer. 2002; 2: 683-693.
5. Könik A, O'Donoghue JA, Wahl RL, Graham MM, Van den Abbeele AD. Theranostics: the role of quantitative nuclear medicine imaging. Semin Radiat Oncol. 2021; 31: 28-36.
6. Michalski MH, Chen X. Molecular imaging in cancer treatment. Eur J Nucl Med Mol Imaging. 2011; 38: 358-377.
7. Vaz SC, Oliveira F, Herrmann K, Veit-Haibach P. Nuclear medicine and molecular imaging advances in the 21st century. Br J Radiol. 2020; 93: 20200095.
8. Mahesh M, Ansari AJ, Mettler FA Jr. Patient exposure from radiologic and nuclear medicine procedures in the United States and worldwide: 2009-2018. Radiology. 2023; 307: e221263.

9. Sgouros G, Bodei L, McDevitt MR, Nedrow JR. Radiopharmaceutical therapy in cancer: clinical advances and challenges. Nat Rev Drug Discov. 2020; 19: 589-608.
10. Strosberg J, El-Haddad G, Wolin E, Hendifar A, Yao J, Chasen B, et al. Phase 3 trial of ^{177}Lu-Dotatate for midgut neuroendocrine tumors. N Engl J Med. 2017; 376: 125-135.
11. Sartor O, de Bono J, Chi KN, Fizazi K, Herrmann K, Rahbar K, et al. Lutetium-177-PSMA-617 for metastatic castration-resistant prostate cancer. N Engl J Med. 2021; 385: 1091-103.
12. Parker C, Nilsson S, Heinrich D, Helle SI, O'Sullivan JM, Fosså SD, et al. Alpha emitter radium-223 and survival in metastatic prostate cancer. N Engl J Med. 2013; 369: 213-223.
13. Ljungberg M, Celler A, Konijnenberg MW, Eckerman KF, Dewaraja YK, Sjögreen-Gleisner K, et al. MIRD Pamphlet No. 26: Joint EANM/MIRD guidelines for quantitative ^{177}Lu SPECT applied for dosimetry of radiopharmaceutical therapy. J Nucl Med. 2016; 57: 151-162.
14. Robertson AKH, Ramogida CF, Rodríguez-Rodríguez C, Blinder S, Kunz P, Sossi V, et al. Multi-isotope SPECT imaging of the ^{225}Ac decay chain: feasibility studies. Phys Med Biol. 2017; 62: 4406-4420.
15. Burkett BJ, Bartlett DJ, McGarrah PW, Lewis AR, Johnson DR, Berberoğlu K, et al. A review of theranostics: perspectives on emerging approaches and clinical advancements. Radiol Imaging Cancer. 2023; 5: e220157.
16. Peterson TE, Furenlid LR. SPECT detectors: the Anger Camera and beyond. Phys Med Biol. 2011; 56: R145-82.
17. Van Audenhaege K, Van Holen R, Vandenberghe S, Vanhove C, Metzler SD, Moore SC. Review of SPECT collimator selection, optimization, and fabrication for clinical and preclinical imaging. Med Phys. 2015; 42: 4796-4813.
18. Ljungberg M, Pretorius PH. SPECT/CT: an update on technological developments and clinical applications. Br J Radiol. 2018; 91: 20160402.
19. Dewaraja YK, Ljungberg M, Green AJ, Zanzonico PB, Frey EC. MIRD Pamphlet No. 24: guidelines for quantitative ^{131}I SPECT in dosimetry applications. J Nucl Med. 2013; 54: 2182-2188.
20. Hutton BF, Buvat I, Beekman FJ. Review and current status of SPECT scatter correction. Phys Med Biol. 2011; 56: R85-R112.
21. Beijst C, Elschot M, Viergever MA, de Jong HW. A parallel-cone collimator for high-energy SPECT. J Nucl Med. 2015; 56: 476-82.
22. Meikle SR, Sossi V, Roncali E, Cherry SR, Banati R, Mankoff D, et al. Quantitative PET in the 2020s: a roadmap. Phys Med Biol. 2021; 66: 06RM01.
23. Vaquero JJ, Kinahan P. Positron emission tomography: current challenges and opportunities for technological advances in clinical and preclinical imaging systems. Annu Rev Biomed Eng. 2015; 17: 385-414.
24. Surti S. Update on time-of-flight PET imaging. J Nucl Med. 2015; 56: 98-105.
25. Lois C, Jakoby BW, Long MJ, Hubner KF, Barker DW, Casey ME, et al. An assessment of the impact of incorporating time-of-flight information into clinical PET/CT imaging. J Nucl Med. 2010; 51: 237-245.
26. Kadrmas DJ, Casey ME, Conti M, Jakoby BW, Lois C, Townsend DW. Impact of time-of-flight on PET tumor detection. J Nucl Med. 2009; 50: 1315-1323.
27. Conti M. Focus on time-of-flight PET: the benefits of improved time resolution. Eur J Nucl Med Mol Imaging. 2011; 38: 1147-1157.
28. Wong WH, Mullani NA, Philippe EA, Hartz R, Gould KL. Image improvement and design optimization of the time-of-flight PET. J Nucl Med. 1983; 24: 52-60.
29. Cherry SR, Jones T, Karp JS, Qi J, Moses WW, Badawi RD. Total-body PET: maximizing sensitivity to create new opportunities for clinical research and patient care. J Nucl Med. 2018; 59: 3-12.
30. Badawi RD, Shi H, Hu P, Chen S, Xu T, Price PM, et al. First human imaging studies with the EXPLORER total-body PET scanner. J Nucl Med. 2019; 60: 299-303.
31. Spencer BA, Berg E, Schmall JP, Omidvari N, Leung EK, Abdelhafez YG, et al. Performance evaluation of the uEXPLORER total-body PET/CT scanner based on NEMA NU 2-2018 with additional tests to characterize PET scanners with a long axial field of view. J Nucl Med. 2021; 62: 861-870.
32. Prenosil GA, Sari H, Fürstner M, Afshar-Oromieh A, Shi K, Rominger A, et al. Performance characteristics of the Biograph Vision Quadra PET/CT system with a long axial field of view using the NEMA NU 2-2018 standard. J Nucl Med. 2022; 63: 476-484.
33. Müller C, Vermeulen C, Köster U, et al. Alpha-PET with terbium-149: evidence and perspectives for radiotheragnostics. *EJNMMI Radiopharm Chem*. 2017;1(1):5.
34. Beyer GJ, Miederer M, Vranješ-Đurić S, Čomor JJ, Künzi G, Hartley O, et al. Targeted alpha therapy in vivo: direct evidence for single cancer cell kill using ^{149}Tb-rituximab. Eur J Nucl Med Mol Imaging. 2004; 31: 547-554.
35. D'Arienzo M. Emission of β^+ particles via internal pair production in the 0^+-0^+ transition of ^{90}Zr: historical background and current applications in nuclear medicine imaging. Atoms. 2013; 1: 2-12.
36. Gates VL, Esmail AAH, Marshall K, Spies S, Salem R. Internal pair production of ^{90}Y permits hepatic localization of microspheres using routine PET: proof of concept. J Nucl Med. 2011; 52: 72-76.
37. Kao YH, Tan EH, Lim KY, Ng CE, Goh SW. Yttrium-90 internal pair production imaging using first generation PET/CT provides high-resolution images for qualitative diagnostic purposes. Br J Radiol. 2012; 85: 1018-1019.
38. Lhommel R, van Elmbt L, Goffette P, Van den Eynde M, Jamar F, Pauwels S, et al. Feasibility of ^{90}Y TOF PET-based dosimetry in liver metastasis therapy using SIR-Spheres. Eur J Nucl Med Mol Imaging. 2010; 37: 1654-1662.
39. Selwyn RG, Nickles RJ, Thomadsen BR, DeWerd LA, Micka JA. A new internal pair production branching ratio of ^{90}Y: the development of a non-destructive assay for ^{90}Y and ^{90}Sr. Appl Radiat Isot. 2007; 65: 318-327.
40. Pasciak AS, Bourgeois AC, McKinney JM, Chang TT, Osborne DR, Acuff SN, et al. Radioembolization and the dynamic role of ^{90}Y PET/CT. Front Oncol. 2014; 4: 38.
41. van Elmbt L, Vandenberghe S, Walrand S, Pauwels S, Jamar F. Comparison of yttrium-90 quantitative imaging by TOF and non-TOF PET in a phantom of liver selective internal radiotherapy. Phys Med Biol. 2011; 56: 6759-6777.
42. Lyu Q, Neph R, Sheng K. Tomographic detection of photon pairs produced from high-energy X-rays for the monitoring of radiotherapy dosing. Nat Biomed Eng. 2023; 7: 323-34.
43. Bodaghi Hosseinabadi R, Rajabi H. Real-time dosimetry in lung cancer radiotherapy using PET imaging of positrons induced by gold nanoparticles. J Radiat Res Appl Sci. 2025; 18: 101361.
44. Delpassand ES, Tworowska I, Esfandiari R, Torgue J, Hurt J, Shafie A, et al. Targeted α-emitter therapy with ^{212}Pb-DOTAMTATE for the treatment of metastatic SSTR-expressing neuroendocrine tumors: first-in-humans dose-escalation clinical trial. J Nucl Med. 2022; 63: 1326-1333.
45. Strosberg JR, Naqvi S, Cohn AL, Delpassand ES, Wagner VJ, Tworowska I, et al. Safety, tolerability and efficacy of ^{212}Pb-DOTAMTATE as a targeted alpha therapy for subjects with unresectable or metastatic somatostatin receptor-expressing gastroenteropancreatic neuroendocrine tumors (SSTR+ GEP-NETs): a phase 2 study. J Clin Oncol. 2024; 42: 4020.
46. Griffiths MR, Pattison DA, Latter M, Kuan K, Taylor S, Tieu W, et al. First-in-human ^{212}Pb-PSMA-targeted α-therapy SPECT/CT imaging in a patient with metastatic castration-resistant prostate cancer. J Nucl Med. 2024; 65: 664.
47. Berner K, Hernes E, Kvassheim M, Revheim ME, Bastiansen J, Selboe S, et al. First-in-human phase 0 study of AB001, a prostate-specific membrane antigen-targeted ^{212}Pb radioligand, in patients with metastatic castration-resistant prostate cancer. J Nucl Med. 2025; 66: 732-8.
48. Berckmans Y, Kleynhans J, Van Mechelen S, Goffin K, Baete K, Koole M, et al. Lead radionuclides for theranostic applications in nuclear medicine: from atom to bedside. Theranostics. 2026; 16: 2887-2917.
49. Banerjee SR, Minn I, Kumar V, Josefsson A, Lisok A, Brummet M, et al. Preclinical evaluation of ^{212}Pb-labeled low-molecular-weight compounds for targeted radiopharmaceutical therapy of prostate cancer. J Nucl Med. 2020; 61: 80-88.
50. Ramonaheng K, Qebetu M, Banda K, Goorhoo P, Legodi K, Mdanda S, et al. Advances in dosimetry and imaging for ^{203}Pb and ^{212}Pb radiotheranostics. Semin Nucl Med. 2025; 55: 1011-1031.
51. Juzeniene A, Stenberg VY, Bruland ØS, Revheim ME, Larsen RH. Dual targeting with ^{224}Ra/^{212}Pb-conjugates for targeted alpha therapy of disseminated cancers: a conceptual approach. Front Med (Lausanne). 2023; 9: 1051825.
52. Kästner D, Hartmann H, Freudenberg R, Pretze M, Brogsitter C, Schultz MK, et al. Gamma camera imaging characteristics of ^{203}/^{212}Pb as a theragnostic pair for targeted alpha therapy: a feasibility study. EJNMMI Phys. 2025; 12: 50.
53. Kvassheim M, Revheim MR, Stokke C. Quantitative SPECT/CT imaging of lead-212: a phantom study. EJNMMI Phys. 2022; 9: 52.
54. [Internet] National Nuclear Data Center. NuDat 3.0. Brookhaven National Laboratory. https://www.nndc.bnl.gov/nudat/
55. Griffiths MR, Campbell L, Latter M, et al. ^{212}Pb PSMA imaging by pair production PET confirms localisation of alpha emissions within tumour lesions. EANM'25. 2025; OP290: S127.
56. Hansen AR, Ngai S, Goh JC, Wyld D, Gan CL, Katchel L, et al. Results from the Phase 1b dose escalation of ^{212}Pb-ADVC001 in metastatic castration-resistant prostate cancer (mCRPC) and novel ^{212}Pb PET clinical imaging. J Med Imaging Radiat Sci. 2026; 57: 102292.
57. Karp JS, Surti S, Daube-Witherspoon ME, Muehllehner G. Benefit of time-of-flight in PET: experimental and clinical results. J Nucl Med. 2008; 49: 462-70.
58. Akamatsu G, Ishikawa K, Mitsumoto K, Taniguchi T, Ohya N, Baba S, et al. Improvement in PET/CT image quality with a combination of point-spread function and time-of-flight in relation to reconstruction parameters. J Nucl Med. 2012; 53: 1716-22.
59. Chaudhari AS, Mittra E, Davidzon GA, Gulaka P, Gandhi H, Brown A, et al. Low-count whole-body PET with deep learning in a multicenter and externally validated study. NPJ Digit Med. 2021; 4: 127.
60. Moskal P, Baran J, Bass S, Choiński J, Chug N, Curceanu C, et al. Positronium image of the human brain in vivo. Sci Adv. 2024; 10: eadp2840.
61. Conti M, Eriksson L. Physics of pure and non-pure positron emitters for PET: a review and a discussion. EJNMMI Phys. 2016; 3: 8.
62. Abuelhia E, Kacperski K, Spyrou NM. Three-photon annihilation in PET: 2D imaging experiments. J Radioanal Nucl Chem. 2007; 271: 489-95.
63. Berger MJ, Hubbell JH, Seltzer SM, Chang J, Coursey JS, Sukumar R, et al. XCOM: photon cross sections database. NIST Standard Reference Database 8 (XGAM). Gaithersburg, MD: National Institute of Standards and Technology; 2010.
64. Jan S, Santin G, Strul D, Staelens S, Assié K, Autret D, et al. GATE: a simulation toolkit for PET and SPECT. Phys Med Biol. 2004; 49: 4543-4561.
65. Levin CS, Hoffman EJ. Calculation of positron range and its effect on the fundamental limit of positron emission tomography system spatial resolution. Phys Med Biol. 1999; 44: 781-799.

66. Osytek KM, Blower PJ, Costa IM, Smith GE, Abbate V, Terry SYA. In vitro proof of concept studies of radiotoxicity from Auger electron-emitter thallium-201. EJNMMI Res. 2021; 11: 63.
67. Atkins HL, Budinger TF, Lebowitz E, Ansari AN, Greene MW, Fairchild RG, et al. Thallium-201 for medical use. Part 3: human distribution and physical imaging properties. J Nucl Med. 1977; 18: 133-40.